universe

MDPI

Communication

Multi-Periodicity of High-Frequency Type III Bursts as a Signature of the Fragmented Magnetic Reconnection

Marian Karlický [1,*] and Ján Rybák [2]

[1] Astronomical Institute of the Czech Academy of Sciences, Fričova 298, CZ-251 65 Ondrejov, Czech Republic
[2] Astronomical Institute, Slovak Academy of Sciences, SK-05960 Tatranska Lomnica, Slovakia
* Correspondence: karlicky@asu.cas.cz

Abstract: Using the radio spectra of the 2 April 2022 eruptive flare, we analyze a group of high-frequency type III bursts by our new wavelet method. In this analysis, we found a multi-periodicity of these bursts that is interpreted by the electron beams accelerated in the fragmented magnetic reconnection in the rising magnetic rope. We propose that each period in these type III bursts is a result of the periodic interaction of sub-ropes formed in the rising magnetic rope. In each interaction, the period depends on the diameter of interacting sub-ropes and local Alfvén velocity. This interpretation is supported by detection of the specific EUV structure which was, according to our knowledge, observed for the first time. All proposed processes occur in the rising magnetic rope. Thus, this flare deviates from the standard flare model, where the main magnetic reconnection is located below the rising magnetic rope.

Keywords: sun; flares; radio radiation

check for updates

Citation: Karlický, M.; Rybák, J. Multi-Periodicity of High-Frequency Type III Bursts as a Signature of the Fragmented Magnetic Reconnection. *Universe* **2023**, *9*, 92. https://doi.org/10.3390/universe9020092

Academic Editor: Baolin Tan

Received: 9 January 2023
Revised: 1 February 2023
Accepted: 6 February 2023
Published: 9 February 2023

Copyright: © 2023 by the authors. Licensee MDPI, Basel, Switzerland. This article is an open access article distributed under the terms and conditions of the Creative Commons Attribution (CC BY) license (https://creativecommons.org/licenses/by/4.0/).

1. Introduction

Solar flares are the most powerful events in the solar system. The strongest flares are associated with coronal mass ejections and the acceleration of particles into interplanetary space. From the physical point of view, solar flares are explosive phenomena in the solar atmosphere, in which the energy accumulated in the magnetic field and electric currents is rapidly transformed into plasma heating, plasma flows, accelerated particles and emission in a broad range of electromagnetic waves: from radio, through optical, UV, X-rays to gamma-rays. For more details, see the reviews [1–6]. The most powerful flares are the eruptive flares that are described by the so-called standard CSHKP flare model [7–10] or by its generalized three-dimensional version [11–13]. In this model, the magnetic rope, carrying the cold and dense filament, is ejected due to toroidal or kink instabilities. Then, below the rising magnetic rope, the narrow current sheet is formed where the main energetic process (magnetic reconnection) occurs. Except for some papers (e.g., [14]), the energetic flare processes in the rising magnetic rope are not considered.

In radio, the eruptive flares are associated with several types of bursts (type II, III, IV, V, J, U) and their fine structures [15]. Among them, there are the high-frequency type III bursts with the normal and reverse frequency drifts that are interpreted as those generated by electron beams with the plasma emission mechanism. While in the normal drifting type III bursts the electron beams are propagating upwards in the solar atmosphere, in the reverse drifting bursts, the beams bombard the dense layers of the solar atmosphere and generate the hard X-ray emission.

In this paper, we analyze an interesting group of the type III bursts observed during the 2 April 2022 flare. Using our new method, we detected multi-periodicity in these bursts. We interpret this multi-periodicity by fragmented reconnection. We support our interpretation with a unique EUV structure. Contrary to the standard flare model, the proposed processes happen inside the rising magnetic rope.

2. Data

We used data from three different radiospectrographs: the ORFEES radiospectrograph working in the 150–1000 MHz range with resolutions of 1.0 s and 0.98 MHz (publicly available data, Observation Radio Frequence pour l'Etude des Eruptions Solaires radiospectrograph, Nancay, France), and the Ondřejov radiospectrographs working in the ranges 800–2000 MHz and 2000–5000 MHz with resolutions of 0.01 s and 4.7 MHz, and 0.01 s and 11.7 MHz [16], respectively. For comparison with radio, we used X-ray and EUV observations from the FERMI [17] and SDO/AIA [18] instruments.

2.1. Data Description

On 2 April 2022, the M3.9 flare occurred in NOAA AR 2975. According to the GOES observation, its start was at 12:56 UT, its maximum was at 13:55 UT and its end was at 14:44 UT. A global overview of this flare in hard X-ray and radio observations is shown in Figures 1 and 2. To see more details, in Figure 3, the 800–5000 MHz spectrum in the 13:22:50–13:25:50 UT time interval is shown. Here, we can see the positively drifting type III bursts (mostly at higher frequencies) as well as the negatively drifting type III bursts (mostly at lower frequencies). The most interesting part of the spectrum is at about 1400 MHz and about 13:25 UT, where type III bursts start to drift to higher and lower frequencies. At this bifurcation region with a frequency of about 1400 MHz, electron beams, generating type III bursts, are accelerated and propagate to lower heights with higher density (positive frequency drift) and to higher heights with a lower density (negative frequency drift). Considering the plasma emission mechanism of the type III burst generation for the emission on the fundamental frequency, the plasma density in the bifurcation (acceleration region) can be estimated as 2.4×10^{10} cm^{-3}. On the other hand, for the emission on the harmonic frequency, this density is 6.0×10^{9} cm^{-3}. All these bursts were followed in the 1000–4000 MHz range by a broadband continuum that was associated with the hard X-ray flux enhancement (see Figure 1). In the 800–5000 MHz range at times after 13:32 UT until the flare end, only a broadband continuum with decreasing radio flux was observed. On lower radio frequencies (ORFEES spectrum), the type III bursts and pulsations were recorded in the 300–800 MHz range at 13:21–13:29 UT.

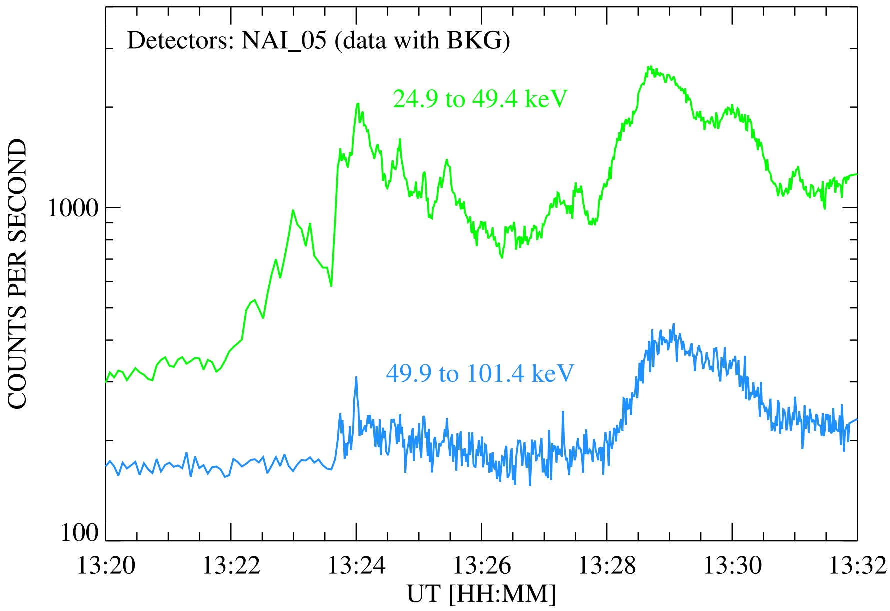

Figure 1. *Cont.*

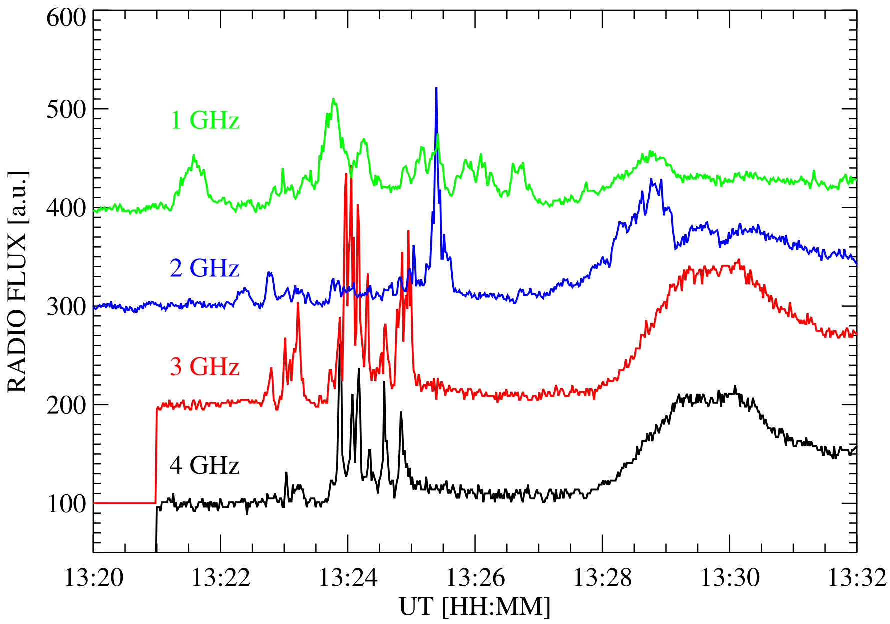

Figure 1. The X-ray and radio fluxes of the 2 April 2022 flare in the time interval 13:20–13:32 UT. (**Upper**) panel: FERMI X-ray fluxes in two energy channels (24.9–49.4 and 49.9–101.4 keV). (**Bottom**) panel: the radio fluxes at 4 GHz (black line), 3 GHz (red), 2 GHz (blue) and 1 GHz (green). The 3 GHz, 2 GHz, 1 GHz fluxes are step by step shifted for 100 a.u. upwards.

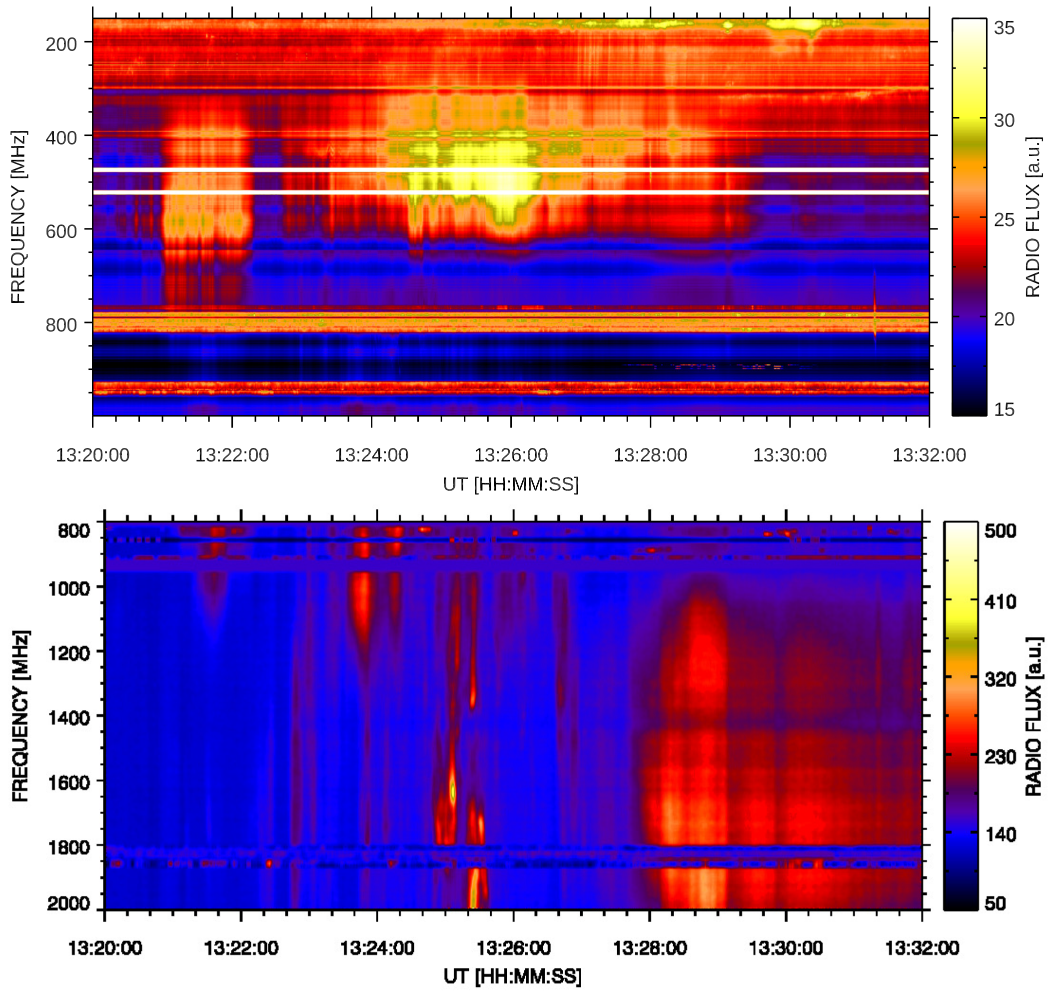

Figure 2. *Cont.*

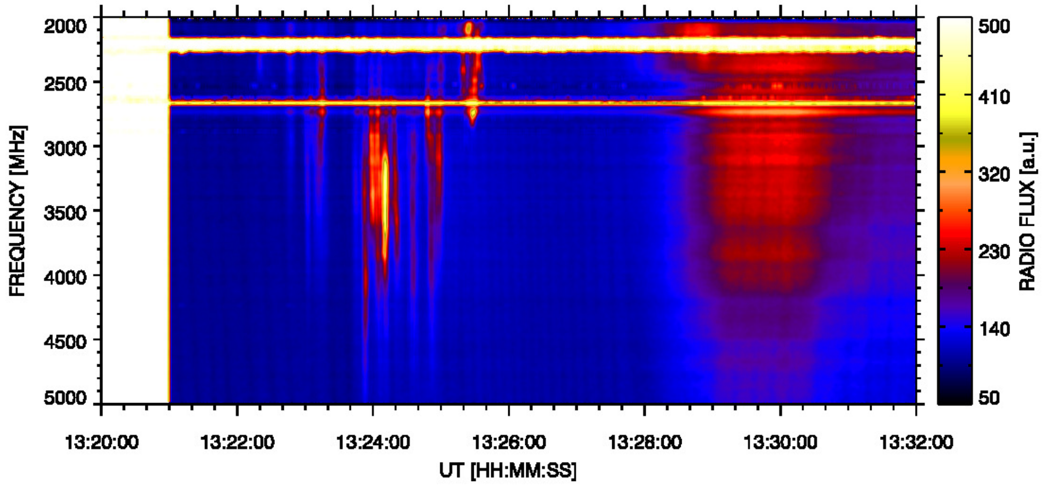

Figure 2. Global 150–5000 MHz radio spectrum in the time interval 13:20–13:32 UT observed during the 2 April 2022 flare: the 150–1000 MHz ORFEES spectrum (**top** panel), the 800–2000 MHz Ondřejov spectrum (**middle** panel), and the 2000–5000 MHz Ondřejov spectrum (**bottom** panel).

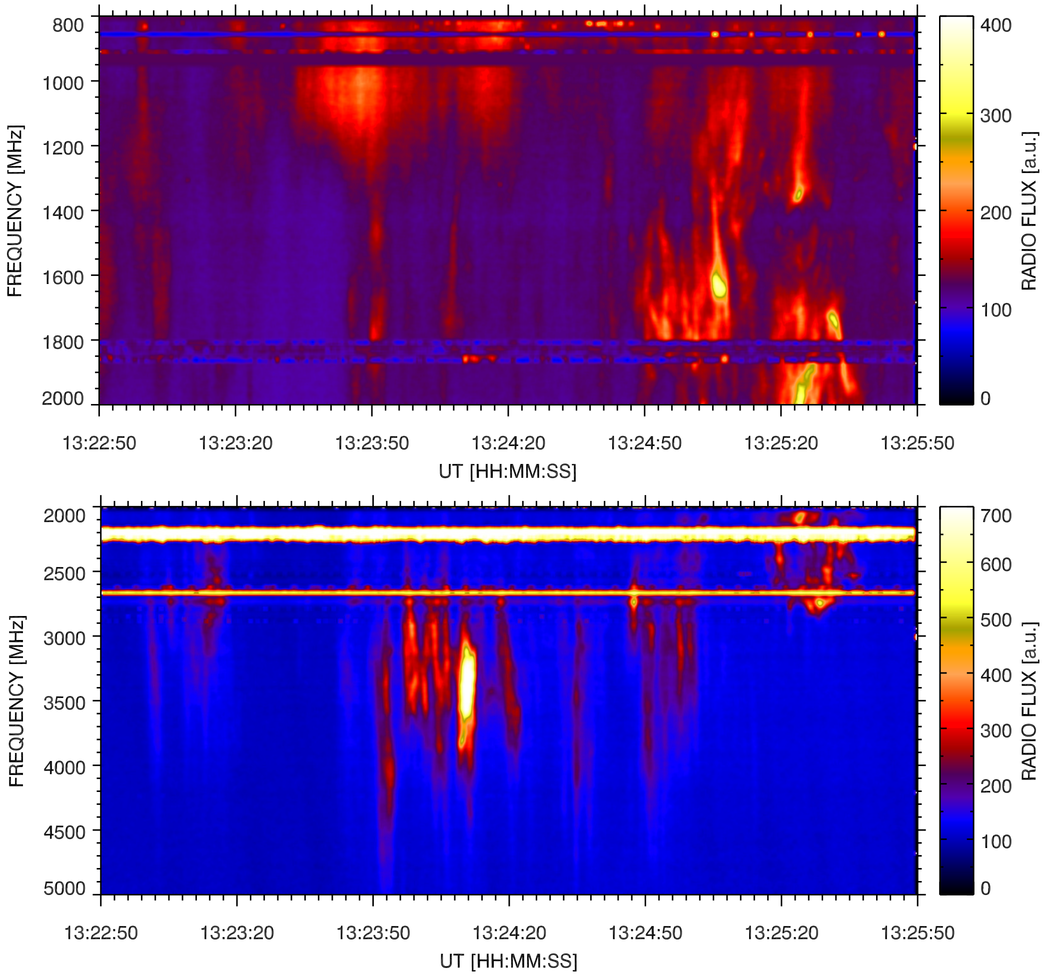

Figure 3. Detailed 800–2000 MHz radio spectrum (**top** panel) and detailed 2000–5000 MHz radio spectrum (**bottom** panel) in the time interval 13:22:50–13:25:50 UT. See the bifurcation region at 1200–1400 MHz and 13:24:50–13:25:30 UT, where type III bursts start to drift to higher or lower frequencies.

2.2. Method of Radio Data Analysis

Before calculations, the Ondřejov radiospectrum data were resampled to 0.1 s temporal resolution. In our analysis, we searched for quasi-periodic variations of radio fluxes in these radio spectra. For this purpose, we used our new method as described in [19,20]. It is based on the wavelet transform (WT) [21] providing a clear detection of the time-frequency evolution of the strong radio wave patterns. The Morlet mother wavelet, consisting of a complex sine wave modulated by a Gaussian, was used to search for radio signal variability, with the non-dimensional frequency ω_0 satisfying the admissibility condition [22]. The WT was calculated for the period range starting from 4 time steps with scales sampled as a fractional power of two with $\delta j = 0.4$. Both the calculated significance of the derived WT periodicities and the cone-of-influence are taken into account as described in [19]. For analysis, the value of the significance level was set to 95%. However, for verification of results, we increased the significance level to 99%. Examples of the WT spectra, calculated using the above-mentioned mother wavelet with the specified values of the WT parameters, are shown in Figures 4 and 5 with two different significance levels of 95% and 99% overplotted on the radio spectrum.

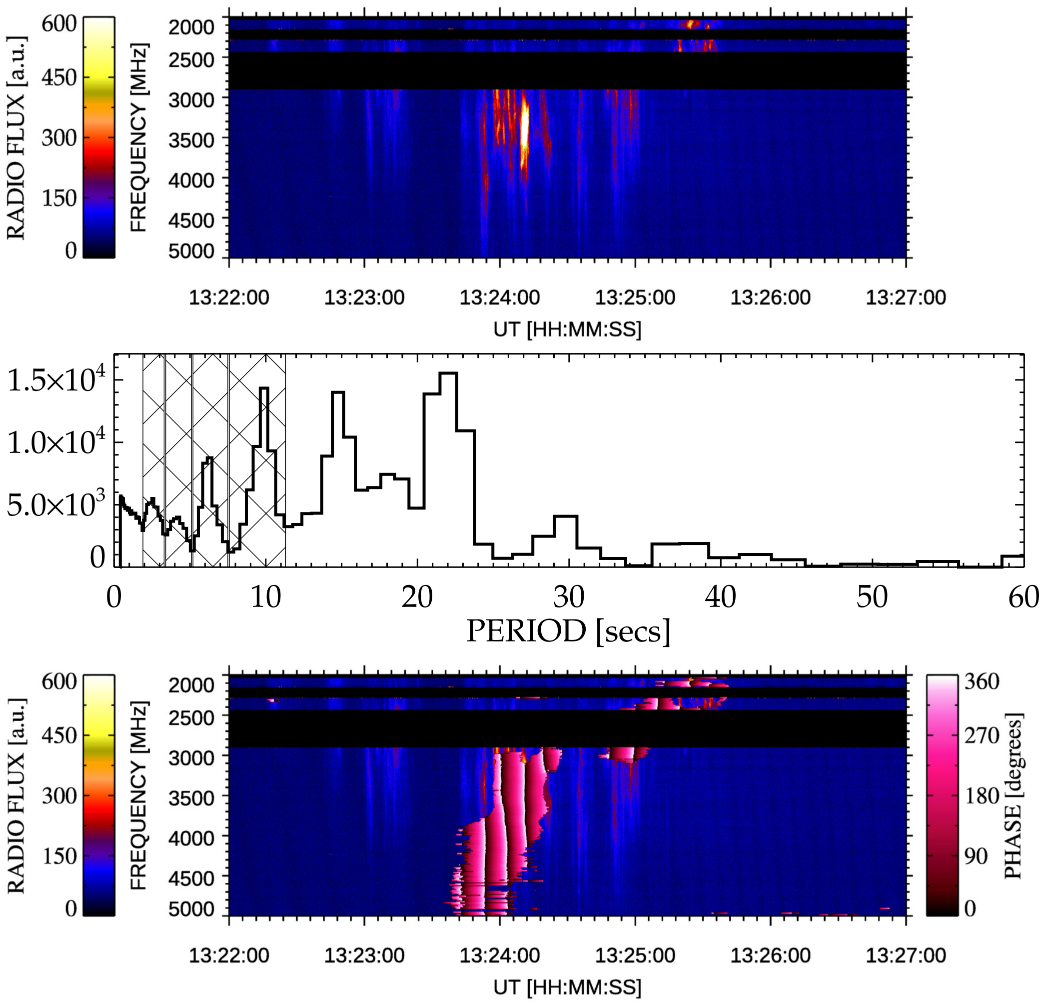

Figure 4. *Cont.*

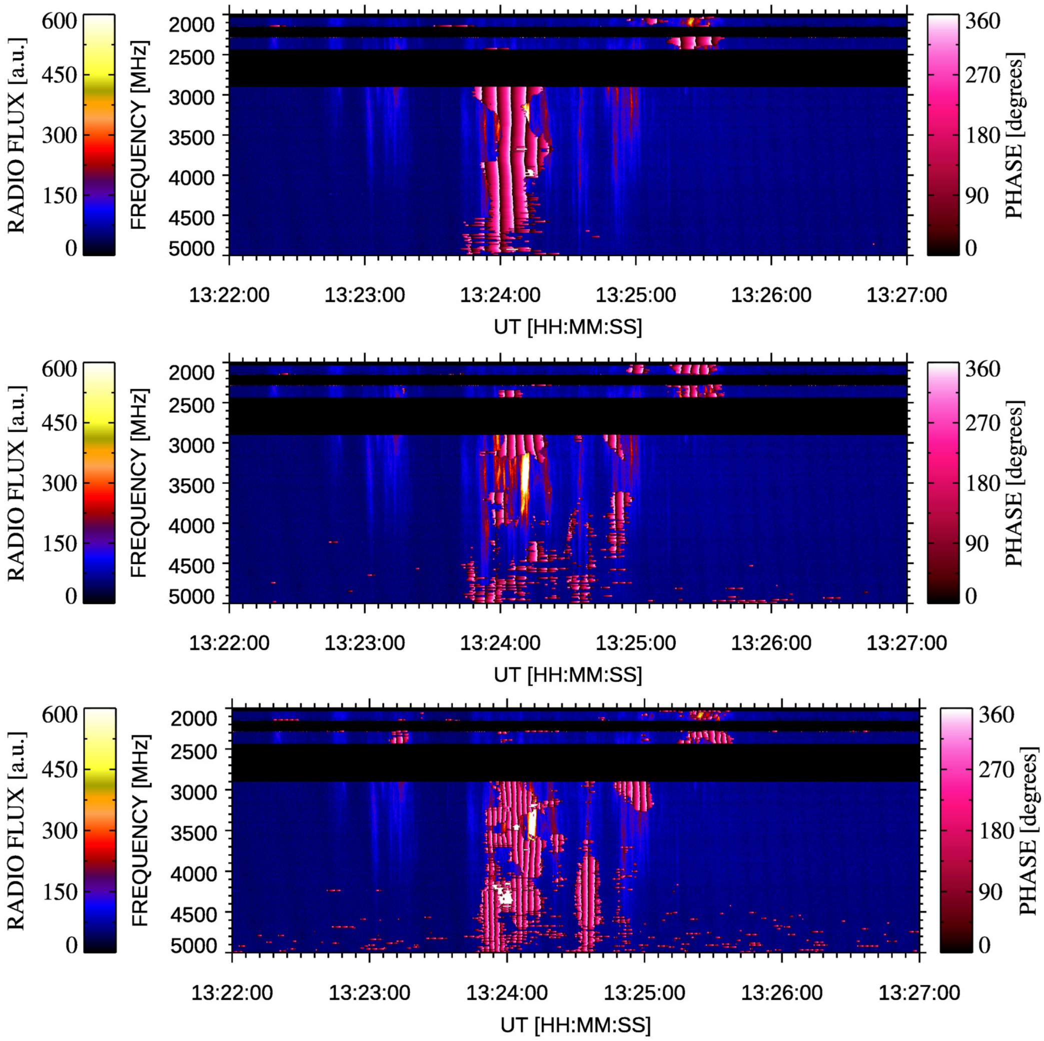

Figure 4. The type III bursts observed on 2 April 2022 in the 2000–5000 MHz range in the 13:22:00–13:27:00 UT time interval: first panel (from **top** to **bottom**): the radio spectrum observed by the Ondřejov radiospectrograph; second panel: histogram of the significant periods detected by the wavelet transform (cross-hatched bands, separated by the vertical lines, mark intervals of periods in bottom phase maps); and bottom four panels: the phase maps (pink areas with the black lines showing the zero phase of oscillations) overplotted on the radio spectrum for periods detected in the ranges of 7.6–11.3, 5.2–7.5, 3.4–5.1 and 1.9–3.3 s. The significance level of these phase maps is 95%.

Similarly as in papers by [19,20,23], at first, we computed the histogram of the detected periods in the whole time-frequency domain of the radio spectra. Each peak in this histogram represents a group of significant periodic signals of a roughly similar period without the location of the periodic signal in the time-frequency domain of the radio spectra.

To show the temporal and frequency location of these periods, for each peak in the period histograms, we made maps of the period phases which we overplotted on the radio spectra. The phases are drawn only in these radiospectrogram time-frequency locations where the periodicities were detected at least with the specified significance. The values of the phases are displayed using their angular values (0–360°).

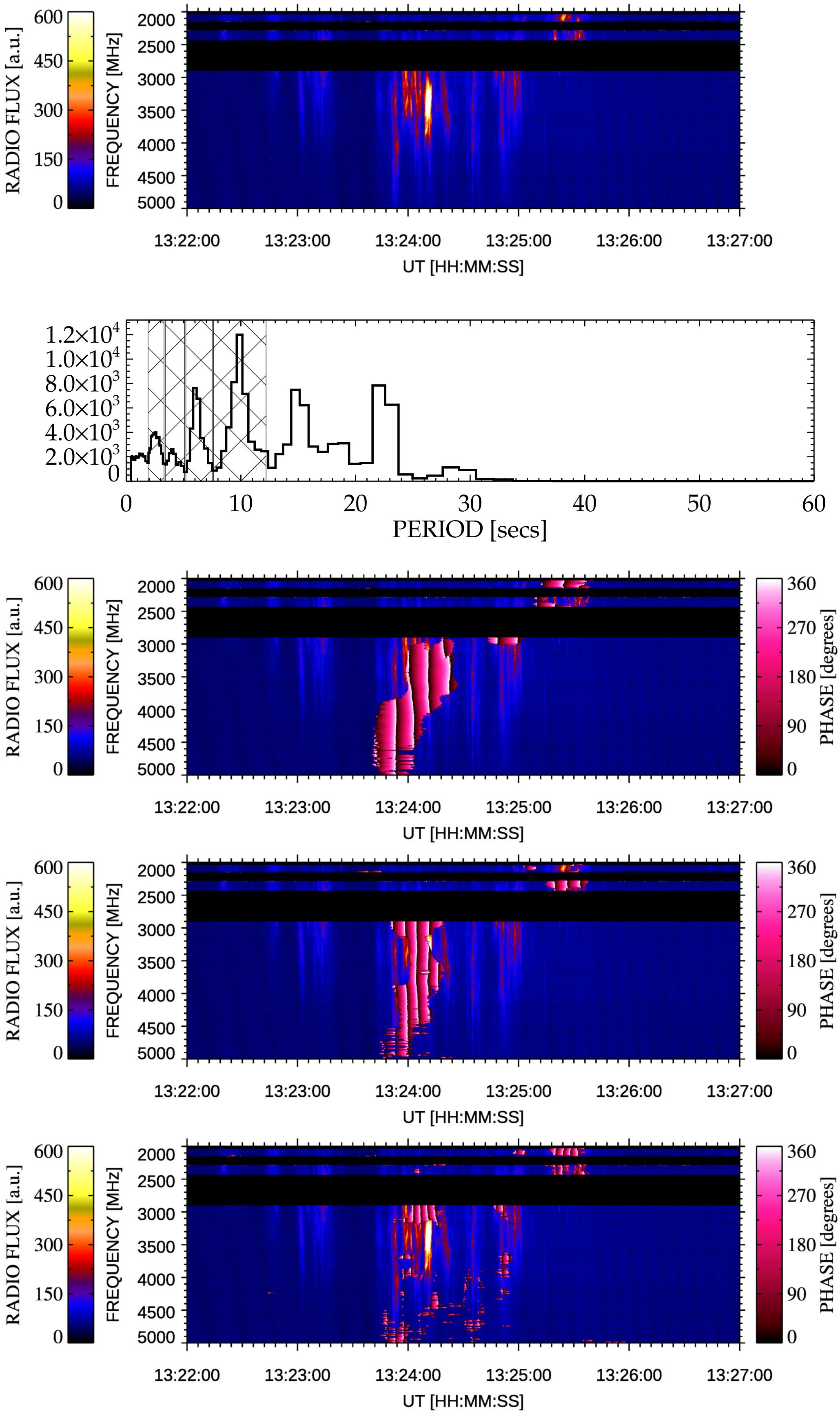

Figure 5. *Cont.*

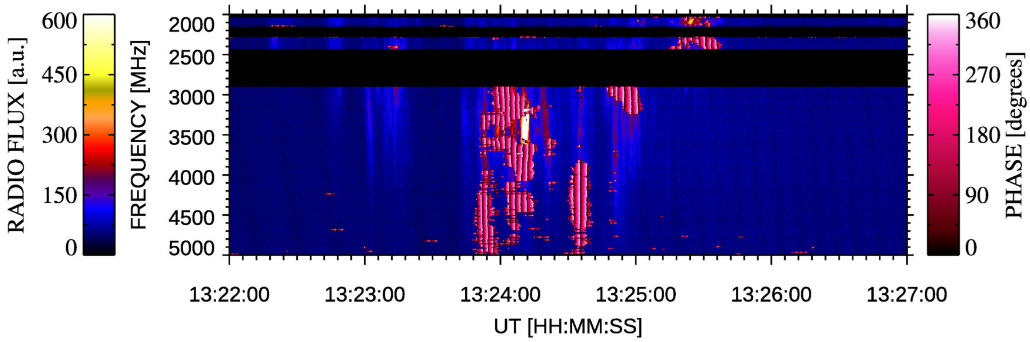

Figure 5. The type III bursts observed on 2 April 2022 in the 2000–5000 MHz range in the 13:22:00–13:27:00 UT time interval: the first panel (from **top** to **bottom**): the radio spectrum observed by the Ondřejov radiospectrograph; second panel: histogram of the significant periods detected by the wavelet transform (cross-hatched bands, separated by vertical lines, mark intervals of periods in bottom phase maps); and bottom four panels: the phase maps (pink areas with the black lines showing the zero phase of oscillations) overplotted on the radio spectrum for periods detected in the ranges of 7.6–12.2, 5.2–7.5, 3.4–5.1 and 1.9–3.3 s. The significance level of these phase maps is 99%.

3. Results

Analyzing radio spectra, we found the most interesting example of the radio flux variations for the group of type III bursts at 13:22–13:27 UT in the 2000–5000 MHz range, where most of them were of the reverse type III bursts. This part of the spectrum together with the histogram of detected periods and four examples of phase maps (for 7.6–11.3, 5.2–7.5, 3.4–5.1 and 1.9–3.3 s quasi-periods given by peaks in the histogram), overplotted on the radio spectrum, are shown in Figure 4.

The histogram of periods and phase maps in Figure 4 show several quasi-periodic processes (for 7.6–11.3, 5.2–7.5, 3.4–5.1 and 1.9–3.3 s quasi-periods) around 13:24 UT, which are especially close to 3 GHz. To verify these results, we increased the significance level from 95% to 99% (Figure 5). As seen by the comparison of Figures 4 and 5, the peaks in histograms and forms of phase maps are nearly the same. To see more details, we made the wavelet analysis of the radio flux at 3 GHz in the 13:22–13:27 UT time interval with the significance levels set to 95% and 99%; see Figure 6. As expected, the area specified by the significance level with 99% is smaller than the area for level 95%. Both these wavelet spectra show a broad interval of periods (0.2–∼10 s) around 13:24 UT.

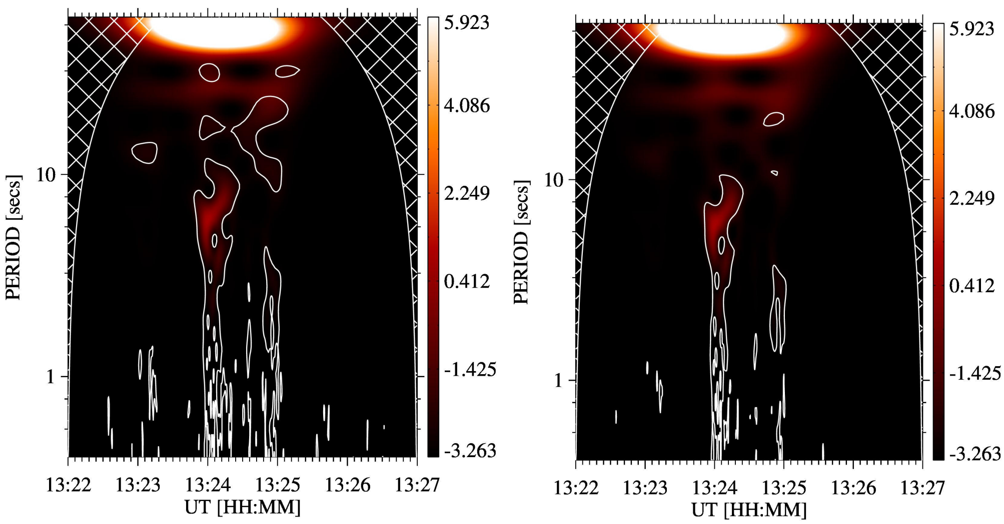

Figure 6. The wavelet power spectrum for the radio flux detected at 3 GHz in the 13:22 – 13:27 UT time interval with the overplotted significance levels (white lines) set to 95% (**left** panel) and 99% (**right** panel).

At the time interval of the analyzed radio spectra, i.e., at the time of the type III bursts, AIA/SDO observations show a huge rising magnetic rope (Figure 7). Three bright features, distributed along the magnetic rope and designated in this figure as HS, indicate a helical magnetic field structure. Most of the flare EUV brightenings (B) are located near the magnetic rope footpoint. Furthermore, during the time interval with type III bursts, we observed a very unique EUV structure in the cross-section of the magnetic rope; see the structure shown by the arrow in Figure 8. This structure has a semi-circular form with four blobs located around a circle. According to our knowledge, such a structure is observed for the first time. Observations in other AIA/SDO EUV lines confirm its reality.

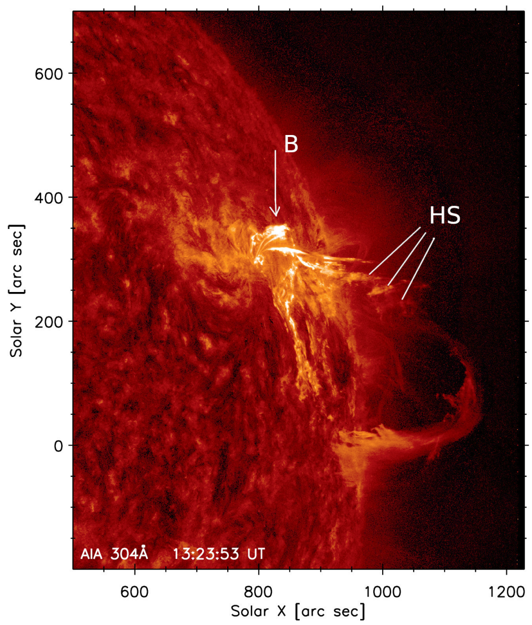

Figure 7. The AIA/SDO 304 Å image was taken at 13:23:53 UT. The letters HS mark three bright features showing the helical structure of the magnetic rope and the letter B brightenings near the magnetic rope footpoint.

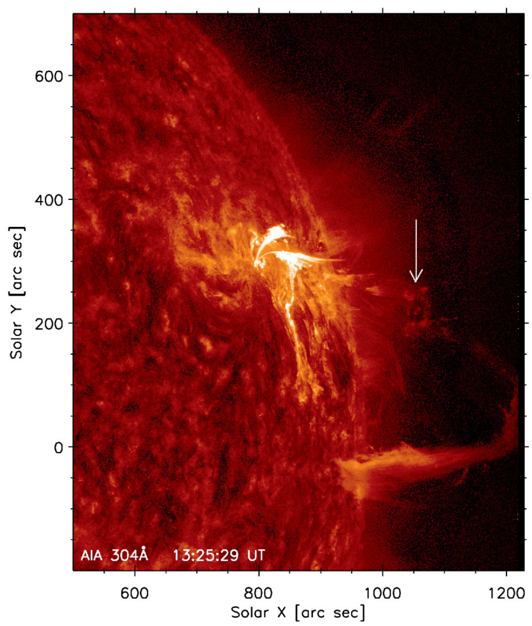

Figure 8. The AIA/SDO 304 Å image taken at 13:25:29 UT. The arrow shows the unique semi-circular structure.

4. Discussion and Conclusions

According to the previous findings (e.g., [15]), the type III bursts with normal (negative) frequency drift are generated by the electron beams propagating upwards in the solar atmosphere and the reverse (positively) drifting type III bursts by beams propagating downwards. In our case, the type III bursts were generated by beams that were accelerated multi-periodically with the quasi-periods in the period ranges 7.6–11.3, 5.2–7.5 and 1.1–1.7 s.

Most of the flare AIA/SDO EUV 304 Å brightenings at the time of the analyzed type III bursts were located near the magnetic rope footpoint. Because the electron beams, generating the type III bursts, propagate along the magnetic field lines, these beams need to be accelerated and propagating inside the magnetic rope.

We interpret the found multi-periodicity of the type III bursts as follows (see also the scenario of processes in Figure 9): the magnetic rope, as shown by its helical structure, carries the electric current. The unique structure, presented in Figure 8, shows that the magnetic rope is not homogeneous in its cross-section. It is structured; it consists of sub-ropes. These sub-ropes can be a result of the rope formation before its rising or they are generated during the rising of the magnetic rope. Some sub-ropes can mutually interact. When the electric current in interacting sub-ropes is oriented in the same direction, then between them in their interaction region, the current sheet is formed. Such a current sheet can be unstable owing to the tearing mode instability [24,25]. As shown by [26,27], this instability can produce a fragmented current sheet, consisting of sub-ropes with different cross-section diameters. Some of these sub-ropes interact. As presented by [28,29], the process of interaction between two sub-rope is periodic. Its period depends on the diameter of cross-sections of the interacting sub-ropes and local Alfvén velocity. Because in our case, the interacting sub-ropes have different cross-sections, the interaction between different sub-ropes has a different period. Each sub-rope interaction periodically accelerates electron beams, and thus, the type III bursts are generated periodically. The beams generating the reverse type III bursts bombard the chromosphere and cause the EUV brightenings there.

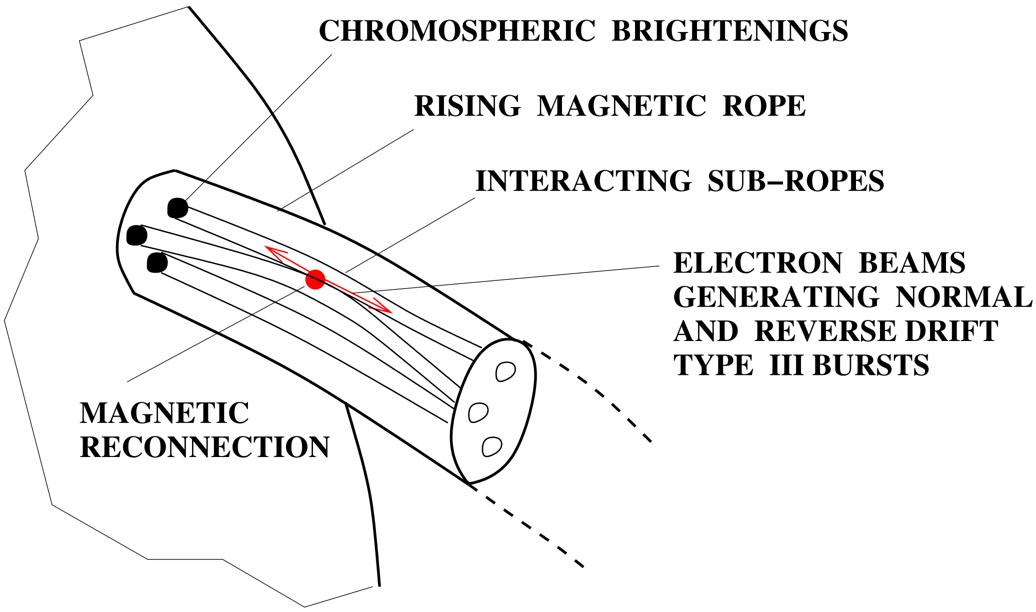

Figure 9. A sketch of the analyzed processes scenario.

The type III bursts analyzed here indicate that they were generated by the fragmented magnetic reconnection inside the rising and unstable magnetic rope. It means that this flare deviates from the standard CSHKP flare model, where the main magnetic reconnection is located below the rising magnetic rope and reconnection processes inside the magnetic rope are not considered. On the other hand, it does not mean that energy release processes according to the standard flare model do not work in later phases of this flare. In future works, it would be interesting to compare the released energy in the rising magnetic rope with that released in the whole flare.

Remark 1. *From a global point of view, the magnetic rope can be considered as half of the toroidal plasma in laboratory systems. Although phenomena in both cases cannot be directly compared, owing to different conditions, the processes such as magnetic islands, local 2D magnetic reconnection and particle acceleration found in the unstable toroidal plasma support our interpretation; see Figures 9, 11, 18–22 and chapter 4.5 in [30].*

Author Contributions: Conceptualization, M.K.; methodology, M.K. and J.R.; software, J.R.; validation, M.K. and J.R.; investigation, M.K.; resources, M.K. and J.R.; data curation, M.K. and J.R.; writing—original draft preparation, M.K.; writing—review and editing, M.K. and J.R.; visualization, M.K. and J.R. All authors have read and agreed to the published version of the manuscript.

Funding: M. K. acknowledges support from the project RVO-67985815 and GA ČR grants 21-16508J and 22-34841S. J.R. acknowledges support by the Science Grant Agency project VEGA 2/0048/20 (Slovakia).

Informed Consent Statement: Not applicable.

Data Availability Statement: The data presented in this study are available on request from the corresponding author.

Acknowledgments: We thank the RSDB service at LESIA/USN (Observatoire de Paris) for making the NRH/ORFEES/NDA data available. Courtesy of NASA/SDO and the AIA science teams. We also thank J. Dudík for the preparation of two AIA/SDO images.

Conflicts of Interest: The authors declare no conflict of interest.

References

1. Priest, E.R.; Forbes, T.G. The magnetic nature of solar flares. *Astron. Astrophys. Rev.* **2002**, *10*, 313–377. [CrossRef]
2. Aschwanden, M.J. Particle acceleration and kinematics in solar flares—A Synthesis of Recent Observations and Theoretical Concepts (Invited Review). *Space Sci. Rev.* **2002**, *101*, 1–227. [CrossRef]
3. Krucker, S.; Battaglia, M.; Cargill, P.J.; Fletcher, L.; Hudson, H.S.; MacKinnon, A.L.; Masuda, S.; Sui, L.; Tomczak, M.; Veronig, A.L.; et al. Hard X-ray emission from the solar corona. *Astron. Astrophys. Rev.* **2008**, *16*, 155–208. [CrossRef]
4. Schrijver, C.J. Driving major solar flares and eruptions: A review. *Adv. Space Res.* **2009**, *43*, 739–755. [CrossRef]
5. Fletcher, L.; Dennis, B.R.; Hudson, H.S.; Krucker, S.; Phillips, K.; Veronig, A.; Battaglia, M.; Bone, L.; Caspi, A.; Chen, Q.; et al. An Observational Overview of Solar Flares. *Space Sci. Rev.* **2011**, *159*, 19–106.
6. Nakariakov, V.M.; Pilipenko, V.; Heilig, B.; Jelínek, P.; Karlický, M.; Klimushkin, D.Y.; Kolotkov, D.Y.; Lee, D.H.; Nisticò, G.; Van Doorsselaere, T.; et al. Magnetohydrodynamic Oscillations in the Solar Corona and Earth's Magnetosphere: Towards Consolidated Understanding. *Space Sci. Rev.* **2016**, *200*, 75–203. [CrossRef]
7. Carmichael, H. A Process for Flares. *NASA Spec. Publ.* **1964**, *50*, 451.
8. Sturrock, P.A. Model of the High-Energy Phase of Solar Flares. *Nature* **1966**, *211*, 695–697. [CrossRef]
9. Hirayama, T. Theoretical Model of Flares and Prominences. I: Evaporating Flare Model. *Sol. Phys.* **1974**, *34*, 323–338. [CrossRef]
10. Kopp, R.A.; Pneuman, G.W. Magnetic reconnection in the corona and the loop prominence phenomenon. *Sol. Phys.* **1976**, *50*, 85–98. [CrossRef]
11. Aulanier, G.; Janvier, M.; Schmieder, B. The standard flare model in three dimensions. I. Strong-to-weak shear transition in post-flare loops. *Astron. Astrophys.* **2012**, *543*, A110. [CrossRef]
12. Janvier, M.; Aulanier, G.; Bommier, V.; Schmieder, B.; Démoulin, P.; Pariat, E. Electric Currents in Flare Ribbons: Observations and Three-dimensional Standard Model. *Astrophys. J.* **2014**, *788*, 60.
13. Dudík, J.; Janvier, M.; Aulanier, G.; Del Zanna, G.; Karlický, M.; Mason, H.E.; Schmieder, B. Slipping Magnetic Reconnection during an X-class Solar Flare Observed by SDO/AIA. *Astrophys. J.* **2014**, *784*, 144.
14. Karlický, M.; Rybák, J. The 2017 September 6 Flare: Radio Bursts and Pulsations in the 22–5000 MHz Range and Associated Phenomena. *Astrophys. J. Suppl. Ser.* **2020**, *250*, 31.
15. Aschwanden, M.J. *Physics of the Solar Corona. An Introduction*; Springer: Berlin/Heidelberg, Germany, 2004.
16. Jiřička, K.; Karlický, M. Narrowband Pulsating Decimeter Structure Observed by the New Ondřejov Solar Radio Spectrograph. *Sol. Phys.* **2008**, *253*, 95–101. [CrossRef]
17. Meegan, C.; Lichti, G.; Bhat, P.N.; Bissaldi, E.; Briggs, M.S.; Connaughton, V.; Diehl, R.; Fishman, G.; Greiner, J.; Hoover, A.S.; et al. The Fermi Gamma-ray Burst Monitor. *Astrophys. J.* **2009**, *702*, 791–804.

18. Lemen, J.R.; Title, A.M.; Akin, D.J.; Boerner, P.F.; Chou, C.; Drake, J.F.; Duncan, D.W.; Edwards, C.G.; Friedlaender, F.M.; Heyman, G.F.; et al. The Atmospheric Imaging Assembly (AIA) on the Solar Dynamics Observatory (SDO). *Sol. Phys.* **2012**, *275*, 17–40. [CrossRef]
19. Karlický, M.; Rybák, J. Oscillation Maps in the Broadband Radio Spectrum of the 1 August 2010 Event. *Sol. Phys.* **2017**, *292*, 1,
20. Karlický, M.; Rybák, J.; Monstein, C. Oscillations in the 45–5000 MHz Radio Spectrum of the 18 April 2014 Flare. *Solar Phys.* **2017**, *292*, 94.
21. Torrence, C.; Compo, G.P. A Practical Guide to Wavelet Analysis. *Bull. Am. Meteorol. Soc.* **1998**, *79*, 61–78. [CrossRef]
22. Farge, M. Wavelet transforms and their applications to turbulence. *Annu. Rev. Fluid Mech.* **1992**, *24*, 395–457. [CrossRef]
23. Karlický, M.; Chen, B.; Gary, D.E.; Kašparová, J.; Rybák, J. Drifting Pulsation Structure at the Very Beginning of the 2017 September 10 Limb Flare. *Astrophys. J.* **2020**, *889*, 72.
24. Loureiro, N.F.; Schekochihin, A.A.; Cowley, S.C. Instability of current sheets and formation of plasmoid chains. *Phys. Plasmas* **2007**, *14*, 100703–100703.
25. Uzdensky, D.A.; Loureiro, N.F.; Schekochihin, A.A. Fast Magnetic Reconnection in the Plasmoid-Dominated Regime. *Phys. Rev. Lett.* **2010**, *105*, 235002. [CrossRef]
26. Shibata, K.; Tanuma, S. Plasmoid-induced-reconnection and fractal reconnection. *Earth Planets Space* **2001**, *53*, 473–482.
27. Karlický, M.; Bárta, M. Successive Merging of Plasmoids and Fragmentation in a Flare Current Sheet and Their X-Ray and Radio Signatures. *Astrophys. J.* **2011**, *733*, 107.
28. Tajima, T.; Sakai, J.; Nakajima, H.; Kosugi, T.; Brunel, F.; Kundu, M.R. Current Loop Coalescence Model of Solar Flares. *Astrophys. J.* **1987**, *321*, 1031. [CrossRef]
29. Sakai, J.I.; de Jager, C. Solar Flares and Collisions Between Current-Carrying Loops Types and Mechanisms of Solar Flares and Coronal Loop Heating. *Space Sci. Rev.* **1996**, *77*, 1–192. [CrossRef]
30. Park, H.K.; Choi, M.J.; Kim, M.; Kim, M.; Lee, J.; Lee, D.; Lee, W.; Yun, G. Advances in physics of the magneto-hydro-dynamic and turbulence-based instabilities in toroidal plasmas via 2-D/3-D visualization. *Rev. Mod. Plasma Phys.* **2022**, *6*, 18. [CrossRef]

Disclaimer/Publisher's Note: The statements, opinions and data contained in all publications are solely those of the individual author(s) and contributor(s) and not of MDPI and/or the editor(s). MDPI and/or the editor(s) disclaim responsibility for any injury to people or property resulting from any ideas, methods, instructions or products referred to in the content.